PAPER

Check for updates

Formate-mediated magnetic superexchange in the model hybrid perovskite [(CH₃)₂NH₂]Cu(HCOO)₃†

Rebecca Scatena, [ID] *[a] Roger D. Johnson,[b] Pascal Manuel[c] and Piero Macchi [ID] [de]

We have investigated the magnetic and electronic structures of crystalline dimethylammonium copper formate [(CH₃)₂NH₂]Cu(HCOO)₃, a model compound that belongs to a wide class of hybrid organic–inorganic perovskites. We present the results of a combined experimental approach, where neutron diffraction and magnetisation measurements were used to solve the ground state magnetic structure in which the same ligand mediates both antiferromagnetic and ferromagnetic interactions, while the electron charge density distribution and orbital occupancy were determined by high-resolution X-ray diffraction. The latter enabled a microscopic analysis of the chemical bonding, from which we established a detailed correlation between the structural, electronic, and magnetic properties of [(CH₃)₂NH₂]Cu(HCOO)₃, demonstrating the primary role of Cu–O bonding in establishing the nature of the exchange. Our results elucidate the mechanism of magnetic exchange mediated by formate anions, from which we examine the applicability of foundational theories of purely inorganic perovskites and define characteristics that the ligands should meet to support the use of the Goodenough–Kanamori–Anderson rules.

Introduction

The discovery of solid-state phenomena and the development of new functional materials are typically underpinned by the application of well-established structure–property relationships. In this regard, an exemplary family of materials is that of inorganic transition metal oxide perovskites with generic chemical formula ABO_3.[1] In these systems, a deep understanding of how the crystal structure is related to materials properties has been developed, alongside exceptional discoveries of technologically important properties such as multiferroicity[2,3] and colossal magnetoresistance.[4,5]

[a] *Department of Physics, Clarendon Laboratory, University of Oxford, Parks Road, Oxford, OX1 3PU, UK. E-mail: rebecca.scatena@physics.ox.ac.uk*

[b] *Department of Physics and Astronomy, University College London, Gower Street, London, WC1E 6BT, UK*

[c] *ISIS Pulsed Neutron and Muon Facility, STFC Rutherford Appleton Laboratory, Chilton, Oxfordshire OX11 0QX, UK*

[d] *Department of Chemistry, Materials, and Chemical Engineering, Polytechnic of Milan, Milan 20131, Italy*

[e] *Istituto Italiano di Tecnologia, Center for Nano Science and Technology CNST@polimi, Milan 20133, Italy*

† Electronic supplementary information (ESI) available: The ESI include a PDF file with: graphs and fitting of magnetization measures, tables of the crystallographic information, fitting of neutron diffraction data, simulated pattern for magnetic structures and table of integrated charges; and CIF files of the charge density multipolar model at 110 K and of the powder neutron diffraction refinements at 1.5 and 10 K. See DOI: 10.1039/d0tc03913f

Compared to the inorganic transition metal oxide perovskites, hybrid organic–inorganic coordination polymers are a relatively young class of materials in which a transition metal is coordinated by polydentate organic ligands forming extended periodic structures.[6] The synthetic conditions, the coordination geometry of the transition metal, the interplay between possible interactions (*i.e.* covalent, ionic, coordinative, hydrogen, and van der Waals), and the chemical and structural characteristics of the ligands, all play a role in the final structure of the material. These parameters, together with the rich variety of organic molecular building blocks, give rise to a vast number of new materials that can be engineered with considerable control. Despite this inherent structural flexibility, coordination polymers whose framework topologies closely emulate that of the well-known inorganic perovskites are receiving considerable attention at present, especially in the field of multiferroics.[7–13] In these cases empirical and semi-empirical structure–property relationships established for the inorganic counterparts might be used to anticipate the behavior of hybrid materials, hence accelerating their discovery and potential application.

To this end, we have explored the relationships between structure and magnetic properties in [(CH₃)₂NH₂]Cu(HCOO)₃ [dimethylammonium copper formate (DMACuF)] – a canonical hybrid organic–inorganic perovskite.[14–16] In DMACuF the perovskite B sites are occupied by Cu^{2+} cations, and the O sites by formate $(HCOO)^-$ molecular anions. Accordingly, six formate ions coordinate the Cu^{2+} cations, which in turn form a 3D pseudo-cubic periodic framework of corner-shared octahedra (Fig. 1a).

12840 | *J. Mater. Chem. C*, 2020, **8**, 12840–12847

This journal is © The Royal Society of Chemistry 2020

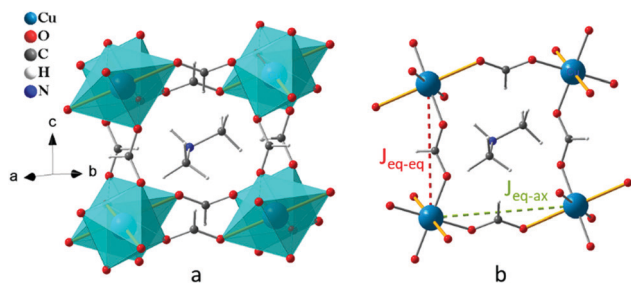**Fig. 1** Crystal structure of $[(CH_3)_2NH_2]Cu(HCOO)_3$ with (a) the $a^-b^-b^-$ octahedral tilt pattern (in Glazer notation)[22] of the ABO_3 perovskite architecture and (b) two geometrically different superexchange pathways. Yellow thick sticks represent JT axes, the red and green dotted lines show respectively symmetric and asymmetric Cu-formate-Cu pathways.

The A sites at the center of the framework voids are occupied by dimethylammonium cations $[(CH_3)_2NH_2]^+$, whose +1 charges balance the charge of the copper formate periodic framework $\{Cu(HCOO)_3^-\}_n$. All $Cu^{II}O_6$ octahedra are centrosymmetric and axially elongated due to the Jahn–Teller (JT) instability of the $3d^9$ Cu^{2+} cations. The JT elongated Cu-formate bonds alternate approximately along the $a + b$ and $a − b$ directions from one Cu^{2+} site to the next, giving rise to alternating asymmetric Cu-formate-Cu pathways (labeled eq–ax) in the ab-plane (Fig. 1b). Short equatorial Cu-formate bonds align approximately along the c direction, forming symmetric Cu-formate-Cu pathways perpendicular to the ab-plane, labeled eq–eq. Hence, there exists two symmetry-inequivalent nearest-neighbor magnetic superexchange (SE) pathways with exchange coupling constants $J_{eq–eq}$ and $J_{eq–ax}$, respectively. Wang et al.[16] reported that the temperature dependent magnetic susceptibility curve of DMACuF (Fig. S1, ESI†) could be fit assuming an $S = 1/2$ 1D Heisenberg model with antiferromagnetic (AFM) $J_{eq–eq} = 77.4(3)$ K. However, muon spin relaxation studies by Baker and coworkers[17] revealed that below $T_N = 5.2$ K the material undergoes 3D long range magnetic order.

The nature of the ab-plane SE interaction $J_{eq–ax}$ responsible for the 3D magnetic order is still the subject of debate. Based on the field dependence of the magnetic susceptibility below T_N, and the fact that AFM coupling is normally observed for SE interactions mediated by molecular building blocks, $J_{eq–ax}$ has been reported to be AFM.[17] Alternatively, based on the foundational Goodenough–Kanamori–Anderson (GKA) rules[18–20] taken from inorganic perovskite research,[21] and density functional theory (DFT) studies,[16] $J_{eq–ax}$ has been reported to be ferromagnetic (FM). Importantly, confirming the latter case would demonstrate that formate ligands can be used to mediate both FM and AFM superexchange.

In this paper, we present a detailed characterization of magnetic and electronic structures in DMACuF aiming to establish empirical microscopic and phenomenological structure–property relationships that can be compared to those valid for the inorganic analogues, and applied to a much broader range of materials. To reach our goal, we have first determined the true ground state magnetic structure of DMACuF by a combination of neutron powder diffraction and single crystal magnetometry. Then, to establish the microscopic origin of the observed

magnetic structure and explore the general validity of the GKA rules in hybrid perovskites, the SE mechanism mediated by formate $HCOO^-$ and its electronic structure were determined by experimental charge density analysis and DFT calculations.

Experimental

Synthesis and crystal growth

All chemicals were purchased commercially and used without further purification. The syntheses were performed in 50 mL Teflon-lined stainless-steel autoclave reactors. 0.0116 g of $Cu(NO_3)_2\cdot 3H_2O$ were dissolved in a mixture of 5.97 g of N,N-dimethylformamide (DMF) and 18.14 g of deionized H_2O. The solution was heated up to 140 °C and maintained at this temperature for 48 h. The reactor was then cooled down to room temperature. The precipitated mixture of CuO and Cu_2O was filtered out and the colorless mother liquors used as solvent for 1.7329 g of $Cu(BF_4)_2\cdot 6H_2O$. The obtained light blue solution was slowly evaporated to produce 1.1327 g of $[(CH_3)_2NH_2]Cu(HCOO)_3$ as light blue prismatic crystals. The product was isolated by filtration and then washed three times with ∼5 °C MeOH. A deuterated sample was prepared for neutron scattering measurements according to the same synthetic strategy but starting from deuterated DMF and deuterated water, and by extending the duration of the solvothermal reaction step to 108 h.

Magnetic susceptibility measurements

Magnetization as a function of applied magnetic field was measured on a 1.56 mg single crystal using a Quantum Design MPMS3. The measurement was carried out at a sample temperature of 2 K, and the magnetic field was swept from $0 \rightarrow +5 \rightarrow −5 \rightarrow 0$ T. The experiment was repeated three times with the magnetic field (H) applied along the three principal crystallographic directions [100], [010], and [001], respectively. The alignment precision was estimated to be $\pm 5°$ due to the limited size of the sample. Regions of linear dependence between magnetization (M) and applied magnetic field (H) were fitted to estimate the main exchange coupling constant $J_{eq–eq}$ by

$$M_i = \frac{g_i^2 \mu_B H}{8 J_{eq–eq}} \cdot \mu_B$$

where g_i is the component of the g-tensor[16] along the magnetization direction, i, derived in the limit of zero magnetic anisotropy, see Fig. S2 (ESI†).

Powder elastic neutron diffraction

Elastic neutron diffraction patterns were collected using WISH, a time-of-flight diffractometer at ISIS, Rutherford Appleton Laboratory, UK. About 1.5 g of polycrystalline $[(CD_3)_2ND_2]Cu(DCOO)_3$ was loaded into a cylindrical vanadium can and placed into an Oxford Instruments cryostat. Diffraction patterns with high counting statistics (3 h) were collected at 10.0 and 1.5 K, above and below T_N. Moreover, 60 min-long data collections were performed at 2.0, 3.0, 3.5, 4.0, 4.5, 5.0 and 5.5 K to extract the

This journal is © The Royal Society of Chemistry 2020

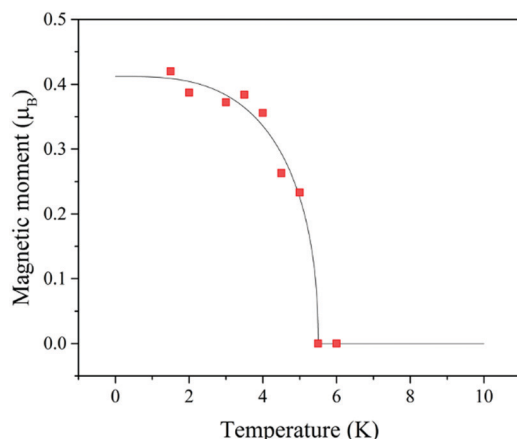*J. Mater. Chem. C*, 2020, **8**, 12840–12847 | **12841**

Fig. 2 Temperature dependence of the ordered magnetic moment throughout the magnetic phase. The black line is drawn as a guide to the eye.

temperature dependence of the magnetic order parameter. Rietveld refinements were performed using FULLPROF against the data measured in detector banks at average 2θ values of $58°$, $90°$, $122°$ and $154°$, each covering $32°$ of the scattering plane. Structural parameters derived from high-resolution single crystal X-ray measurements of a hydrogenated sample at 110 K were used as an initial input. All atoms were refined using isotropic thermal displacement parameters. The thermal parameters of chemically equivalent atoms were constrained to be equal. Candidate magnetic structure models were established by symmetry analysis performed using ISODISTORT,[23] which were systematically tested against the data obtained from the difference between the patterns collected at 1.5 K and 10 K (Fig. 3). The temperature dependence of the main magnetic peak intensity at (001) was extracted by fitting a Gaussian function, which was then expressed in terms of a magnetic moment scaled to the moment refined at 1.5 K (Fig. 2).

High-resolution single-crystal X-ray diffraction and charge density refinement

A single crystal of $[(CH_3)_2NH_2]Cu(HCOO)_3$ with dimensions $363 \times 165 \times 79$ μm was glued to a glass fibre and cooled to 110(2) K using an Oxford Cryostream flow cryostat. Redundant data were collected up to 0.45 Å using an Oxford Diffraction SuperNova area-detector diffractometer employing mirror optics, monochromated, and Al filtered microsource Mo Kα radiation ($\lambda = 0.71073$ Å). CrysAlisPro software was used for the calculation of the collection strategy and for the data reduction. Lorentz, polarization and absorption corrections were applied analytically. The results of a conventional spherical independent atom model (IAM) structural refinement performed using SHELXL[24] provided a starting point for aspherical multipolar model (MM) fitting. The Hansen–Coppens formalism[25] was used for charge density determination as implemented in the XD2016 software.[26] Isotropic extinction was estimated according to the Becker–Coppens equation.[27] All multipoles up to hexadodecapoles, and contraction and expansion parameters κ and κ',

were refined for all non-hydrogen atoms. Independent sets of κ and κ' were refined for different elements. In addition, κ and κ' were independently refined for sp^2 and sp^3 carbon atoms, as well as for axial and equatorial oxygen atoms. Hydrogen atoms were also described non-spherically by refining a dipole along their bond. The hydrogen κ and κ' parameters were constrained to the standard value of 1.2, and anisotropic thermal displacements were estimated using SHADE2.1.[28] Anharmonic motion up to the fourth-order was refined only for Cu atoms, whereas, second order anisotropic thermal parameters were refined for all other atoms. Selected crystallographic data and refinement details are summarized in Table S1 (ESI†). The agreement between structure factors obtained from experiment and fitted multipolar model was evaluated by analysing the residual density distribution. Statistics of the residual density distribution are reported in the ESI† (Fig. S3). The analysis of the electron density was performed using the XDPROP and TOPXD modules of XD2016.

Periodic-DFT simulations

Geometry optimization of the ground state crystal structure of $[(CH_3)_2NH_2]Cu(HCOO)_3$ was carried out in the monoclinic $I2/a$ space group, using CRYSTAL17.[29] The experimental crystal structure determined at 110 K was used as a starting point for the optimization. The unrestricted B3LYP functional was used with basis set 6-31G(d,p). The energies of high- and low-spin configurations were computed to obtain the super-exchange magnetic coupling constants. The simulated electron density distribution was used to obtain a calculated structure factor that was then fitted to the MM by using XD2016[26] and the result was analysed using the XDPROP and TOPXD modules.

Results and discussion

Synthesis and crystallization

The synthesis of dimethylammonium copper formate (DMACuF) starting from Cu^{II} salts and N,N-dimethylformamide (DMF) was optimized to produce large amounts of product with limited volumes of reactor and DMF. We reported a two-steps synthetic strategy which is crucial to produce the deuterated phase. The first reaction step is carried out in solvothermal conditions and leads to hydrolysis of DMF into dimethylammonium $[(CH_3)_2NH_2]^+$ and formate $[HCOO]^-$ via catalytic support from $Cu(NO_3)_2$. The products of the hydrolysis self-assemble into the desired crystal phase upon addition of $Cu(BF_4)_2$. Millimetre-size single crystals were grown by slow evaporation of the solvent.

Crystal structure

High-resolution X-ray diffraction measurements enabled a highly accurate crystal structure refinement of DMACuF (summarised in Tables S1 and S2, ESI†). Peak indexation showed that at 110 K the structure maintained the ambient temperature monoclinic $I2/a$ space group.[30] In this phase Cu^{II} ions are located on inversion centers in the middle of JT axially elongated octahedra characterized by three pairs of Cu–O distances [1.9688(2), 1.9731(2), and 2.4545(3) Å at 110 K]. All formate (HCOO$^-$) ligands bind Cu^{II} ions

12842 | *J. Mater. Chem. C*, 2020, **8**, 12840–12847

This journal is © The Royal Society of Chemistry 2020

Paper

in *anti–anti* fashion with a Cu–O–C angle of about 124°. Cu^{II} ions along *c* are separated by 5.69870(5) Å and connected by symmetric Cu-formate-Cu pathways involving two equatorial Cu–O bonds (denoted eq–eq). Along *a* + *b* and *a* − *b* equivalent directions, Cu^{II} ions are separated by 6.16273(5) Å and connected by asymmetric Cu-formate-Cu pathways involving an equatorial and an axial Cu–O bond (denoted eq–ax). The formate anions that comprise these two pathways have remarkably similar structural parameters with equivalent C–O bond lengths along the symmetric eq–eq path [C1–O1 = 1.2546(2) Å] and two independent C–O bonds along the asymmetric eq–ax path [C2–O2 = 1.2633(3) Å; C2–O3 = 1.2495(4) Å]. C2–O2 and C2–O3 lengths in the eq–ax formate ion remain alike in spite of the very different coordinative interactions that this ligand is exposed to in the crystal.

The structure of deuterated $[(CD_3)_2ND_{1.6}H_{0.4}]Cu(DCOO)_3$ was determined by refinement of the hydrogenated structure (described above) against elastic neutron powder diffraction data collected at 10 K (Fig. S4, ESI†). The deuterated phase was found to be isostructural with the hydrogenated phase (Tables S1 and S2, ESI†). No impurity peaks were detected, showing that the synthesis reported above produced the desired product as a pure phase.

Magnetic structure

The elastic neutron diffractogram measured on cooling below T_N revealed three new Bragg peaks whose temperature evolution was consistent with the magnetic phase transition previously characterized by magnetic susceptibility (Fig. S1, ESI†). These three peaks were therefore assigned to 3D long range magnetic order, and the temperature-dependent trend of the respective magnetic moments (square-root of intensity), is shown in Fig. 2.

The magnetic peaks occurred at small values of scattering vector length $|Q|$ (*i.e.* large *d*-spacing values), and they could be indexed by the *Y*-point propagation vector (0,0,1), defined with respect to the $I2/a$ paramagnetic crystal structure. Symmetry analysis using ISODISTORT[23] gave two irreducible representations for the Cu^{II} lattice: mY_1^- and mY_2^-. With reference to the description of magnetic structures found in the inorganic perovskites, as formulated by Bertaut,[31] the symmetry adapted modes of mY_1^- and mY_2^- can be written as $A_xC_yA_z$ and $C_xA_yC_z$, respectively. Here, C-type describes a magnetic structure of FM chains along the *c* axis (J_{eq-eq}) with AFM coupling in the *ab* plane (J_{eq-ax}), and A-type describes a magnetic structure of AFM chains along *c* with FM coupling in the *ab* plane. The subscripts denote the magnetic moment component, where $x||a$, $y||b$, and $z||c^*$.

The candidate magnetic structures were simulated (Fig. S5, ESI†) and tested against the magnetic diffraction peaks obtained by taking the difference between patterns collected at 1.5 and 10 K, as shown in Fig. 3. The presence of large C-type modes could be ruled out since they produce magnetic intensities at *d*-spacing positions were no peaks were observed (above the detection limit of the experiment). However, A-type modes capture well the data when the magnetic moment is oriented either along the *a* (A_x) or *b* (A_y) crystallographic axes (*R*-factor = 0.592%, χ^2 = 1.53 and
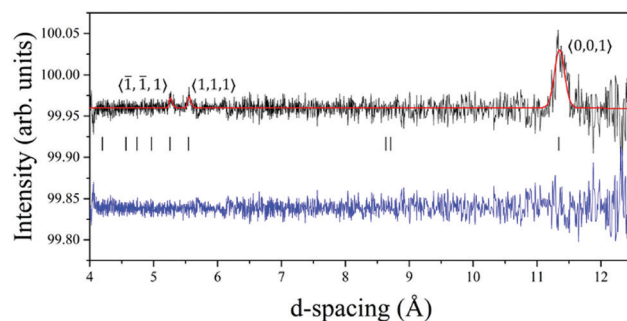

Fig. 3 Powder elastic neutron diffractogram obtained from the difference between diffraction at 1.5 K and 10 K, indexed by propagation vector (0,0,1). Data and fit are shown as black crosses and a red line, respectively, and their difference is drawn as a blue line. Black tick marks show possible Bragg reflection positions for the magnetic structure.

R-factor = 0.885%, χ^2 = 1.53). We note that the A_z mode is inconsistent with the main magnetic peak at (0,0,1), as the magnetic unpolarised neutron diffraction intensity is proportional to the component of the moments perpendicular to Q. Higher resolution magnetic diffraction peaks, which could in theory differentiate between A_x and A_y, were not detected due to their low intensity and overlap with nuclear peaks. At 1.5 K the size of the refined Cu^{II} magnetic moment is significantly reduced: 0.45(24) μ_B instead of 1 μ_B, which is consistent with the effect of quantum fluctuations in low-dimensional AFM systems.[32,33] The magnetic moment temperature dependence extracted from the (0,0,1) intensity (Fig. 2) was scaled to this value.

Measurements of the field-dependent single crystal magnetisation are shown in Fig. 4. For magnetic fields applied along *b* or *c* the magnetisation grows linearly from zero, which is qualitatively consistent with the canting of antiferromagnetic Cu^{II} moments aligned perpendicular to the field *i.e.* parallel to *a*. By contrast, when the magnetic field is applied along the *a* axis the magnetisation maintains very small values until 0.5 T, at which field the magnetisation jumps to a value similar to
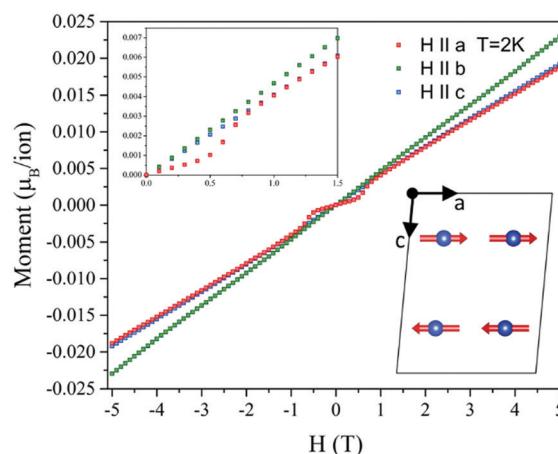

Fig. 4 Magnetisation as a function of magnetic field applied along the principal crystallographic axes for a single crystal of $[(CH_3)_2NH_2]Cu(HCOO)_3$ at 2.0 K. Top left inset: Zoom-in about the spin-flop transition. Bottom right inset: Ground state magnetic structure.

that measured with the field parallel to b or c. For fields of 0.7 T and upwards, the a axis magnetisation follows a linear increase analogous to the b and c field directions. This behaviour is typical of a field-induced spin-flop transition when the field is applied parallel to the direction of the staggered magnetisation (parallel to the magnetic easy axis), hence confirming that the ground state Cu^{II} moments are aligned parallel to a (Inset in Fig. 4). This result is consistent with the spin-flop transition suggested by Wang and coworkers.[16] Hence, the combination of neutron diffraction and magnetisation measurements uniquely identifies an A-type magnetic structure (FM coupled AFM chains) with magnetic moments aligned along the a axis (mY$_1^-$ irreducible representation).

The critical field ($B_C \sim 0.6$ T) provides a direct measure of the small magnetic anisotropy energy, which in the absence of single-ion-anisotropy (Cu^{II}) likely originates in a combination of exchange anisotropy, antisymmetric Dzyaloshinskii–Moriya exchange, and the dipole–dipole interaction. The magnetisation gradient in the linear regimes provides a measure of the 'stiffness' of the antiferromagnetic exchange in this material, J_{eq-eq}, which was estimated to be 71.5(6) K (Fig. S2, ESI†) in excellent agreement with the value found from fitting the magnetic susceptibility.[16] Differences in the gradient for the different field directions were accounted for by the anisotropic g-tensor, which is reported to be maximal along b,[16] as observed.

Charge density distribution

The high-resolution single-crystal X-ray diffraction data measured at 110 K was also used to determine the electron charge density (ρ_{MM}) distribution in DMACuF, using a Hansen–Coppens multipolar model[25] (MM) refined against the measured intensities. The quantum theory of atoms in molecules (QTAIM) topological analysis of ρ_{MM} defines atomic basins and bond trajectories (paths) between pairs of interacting atoms based on the ρ_{MM} gradient.[34] Along a bond path, the point where the gradient of ρ_{MM} goes to zero, called a bond critical point (bcp), can be used to quantify the electron density associated with the interaction. Moreover, the Laplacian and ellipticity of the electron density at the bcp can be used to characterize the bond nature.

In Table 1, we report the electron density properties at the bond critical points of all symmetry-independent nearest-neighbour interactions. The Cu–O bcps have a positive valued Laplacian, indicating that charge density is not concentrated at the centre of the bonds, as expected for coordinative interactions. The situation is different for the intramolecular HCOO$^-$ anion bonds, where negative Laplacian values at their bcps indicate strong covalency. The ellipticity of all bcps is small, demonstrating a cylindrical distribution of the electron density around the bond axes consistent with Sigma-type bonds. The obtained values were validated by comparison with the charge density analysis result obtained for MM fitting of a structure factor calculated from DFT, which are in good agreement (Table 1). Despite being inequivalent by symmetry, the eq–eq and eq–ax formate ligands feature electron density distributions of a similar form. Taken together with the intramolecular bond length

Table 1 Bond critical point properties estimated from experimental multipolar model (Exp. MM) and multipolar model refined against a calculated structure factor (Calc. MM) for [(CH$_3$)$_2$NH$_2$]Cu(HCOO)$_3$. ρ and $\nabla^2\rho$ are the electron density (e per Bohr^3) and its Laplacian (e per Bohr^5). ε is the ellipticity of the electron density distribution. Labelling scheme according to Fig. 6

Bond	Exp. MM			Calc. MM		
	ρ	$\nabla^2\rho$	ε	ρ	$\nabla^2\rho$	ε
Cu–O1	0.075(1)	0.450(1)	0.24	0.070	0.436	0.19
Cu–O2	0.078(1)	0.462(1)	0.24	0.073	0.463	0.16
Cu–O3	0.027(1)	0.117(1)	0.13	0.021	0.095	0.01
O1–C1	0.396(3)	−0.927(3)	0.09	0.378	−1.061	0.04
O2–C2	0.392(4)	−0.966(6)	0.04	0.375	−1.076	0.04
O3–C2	0.399(4)	−0.665(6)	0.04	0.388	−1.098	0.02
N1–C3	0.254(3)	−0.482(2)	0.07	0.236	−0.374	0.01

analysis described above, this observation indicates that the striking differences in the J_{eq-eq} (Cu–O1–C1–O1–Cu) and J_{eq-ax} (Cu–O2–C2–O3–Cu) SE interactions likely originates in the Cu–O bonds and not differing characteristics of the formate ligands. Indeed, the bcp charge densities of the two equatorial bonds, Cu–O1 and Cu–O2, are similar and indicate a strong interaction, whereas the bcp charge density for the Cu–O3 axial bonds (occurring along the JT axis) indicates a much weaker interaction.

Further insight into the ionic or covalent character of the Cu–O interactions can be drawn from the atomic charges integrated within the atomic basins defined by the QTAIM. In DMACuF, all atomic charges are smaller than their formal ionic oxidation states, see Table S3 (ESI†), which indicates a significant level of electron sharing in the interactions – consistent with the covalency apparent in the bcp analysis. Integration of the atomic charges of the eq–eq and eq–ax formate ligands reveals molecular charges of −0.34 and −0.81, respectively. The excess charge density on the eq–ax formate is substantially localized at the axial oxygen (see Fig. 5), further supporting that the key electronic differences between eq–eq and eq–ax SE pathways lie in the Cu–O interactions. The eq–eq formate ligand has a molecular charge that is about 1/3 of the formal charge (−1), which implies a strong electron donation, hence a covalent character, in the equatorial Cu–O bonds. On the contrary, the eq–ax formate ligand has an absolute charge that is only slightly reduced from the formal −1 ionic value, suggesting that the axial Cu–O interactions have a predominately ionic character, in keeping with previous studies.[35,36] These empirical differences in Cu–O covalency, and their relationship to the different J_{eq-eq} and J_{eq-ax} exchange interactions, can be understood in terms of the electronic orbital configuration of the formate and Cu ions, discussed in detail in the following.

Orbital ordering

Electron density deformation maps calculated from the above experimental charge density analysis ($\rho_{MM} - \rho_{spherical}$) allow one to visualize the aspherical part of the charge distribution in terms of regions of electron density depletion or excess. A 2D deformation map of the Cu^{II}O$_4$ equatorial plane is shown in
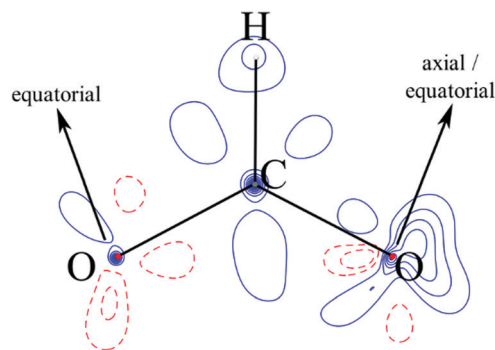
Fig. 5 Difference between charge density distributions of eq–ax formate ion and eq–eq formate ion, where blue and red contours (0.2 e Å^{-3}) represent, respectively, positive and negative regions of electron charge density.
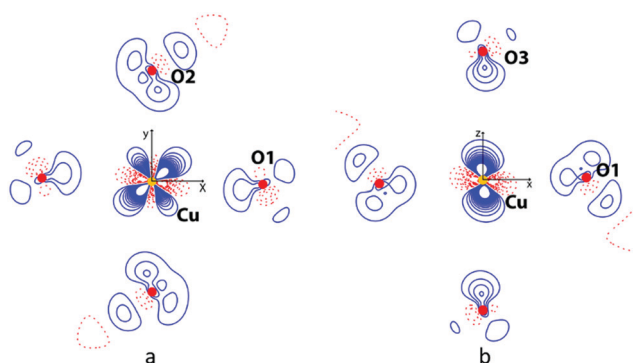

Fig. 6 Experimental static deformation density map (aspherical distribution of the charge density) (a) in the plane defined by Cu^{II} equatorial Cu–O bonds and (b) in the plane containing the JT axis (axial bonds) and two equatorial Cu–O bonds. Blue and red contours (0.2 e Å^{-3}) represent, respectively, the excess and depletion of electron density with respect to the spherical atom distribution.

Fig. 6a, and a map containing equatorial (Cu–O1) and axial (Cu–O3) bonds is shown in Fig. 6b. The relative populations of the multipolar functions used to fit the aspherical electron density distribution around the Cu^{II} ions were converted into d-orbital populations.[37] The result, reported in Table 2, is clearly reflected in the experimental deformation density maps shown in Fig. 6. For example, the partially occupied $d_{x^2-y^2}$ orbital is evident as regions of depleted electron density (red contours) pointing towards the equatorial ligands, while the fully occupied d_{z^2} orbital (*i.e.* $d_{2z^2-x^2-y^2}$) is observed as regions of excess electron density (blue contours) pointing towards the axial ligands. Hence, J_{eq-eq} is mediated *via* two partially occupied $d_{x^2-y^2}$ orbitals, whereas J_{eq-ax} is mediated *via* a partially occupied $d_{x^2-y^2}$ orbital and a fully occupied d_{z^2} orbital. We note that the singularly and fully occupied orbitals may exceed occupancy of 1.0 and 2.0, respectively, since they are based upon d-shaped electron density functions as opposed to exact 3d-orbitals.

The GKA rules are used in inorganic perovskites to predict the sign of magnetic SE coupling mediated *via* oxygen p-orbitals. They depend upon the angle of the metal–oxygen–metal bond and

Table 2 Approximate d-orbital populations from experimental multipolar model refinement (Exp.) and multipolar refinement of theoretical structure factor (Calc.). The names of the orbitals refer to a local orientation of Cu^{II} in which x and y are along equatorial bonds (Cu–O1 and Cu–O2) and z is along the axial bond (Cu–O3 bond)

	$d_{x^2-y^2}$	d_{xz}	d_{xz}	d_{xz}	d_z
Exp.	1.46(3)	2.19(3)	2.16(3)	1.99(3)	2.28(3)
Calc.	1.43	2.21	2.25	2.20	2.14

the electronic configurations of the metal d-orbitals. For 180° bonds, the GKA rules predict strong AFM SE between two half-filled e$_g$ orbitals, and weak FM SE between filled and half-filled e$_g$ orbitals.[21] Our neutron diffraction results showed that J_{eq-eq} is AFM and J_{eq-ax} is FM, which, taken together with the above electron density analysis, is in perfect agreement with the GKA rules.

We suggest that the applicability of the GKA rules, in the 180° bond limit, to the hybrid organic/inorganic perovskites is dependent upon the properties of the ligand molecular orbitals. Specifically, the frontier molecular orbital that primarily mediates SE must effectively emulate oxygen p-orbitals by (a) spanning the molecule to guarantee SE *via* a single molecular orbital, (b) having an appreciable electron density on the extremal atoms that coordinate the metal to allow non-zero overlap with the magnetic orbital of the metal ions, and (c) having symmetric charge density about the molecule middle to ensure that any difference between the two metal–ligand bonds is principally inferred by the electronic configuration of the metal. The molecular orbitals of an isolated formate ion were calculated using gas phase DFT as implemented in Gaussian09.[38] The frontier HOMO and HOMO−1 orbitals are shown in Fig. 7, and clearly satisfy our requirements for the GKA rules to apply.

Simulated magnetic properties

The electronic spin density and magnetic exchange coupling constants were further investigated by DFT calculations. The calculated spin density distribution is shown in Fig. 8 and it corroborates the results of the electron charge density analysis. In particular, the quasi-1D magnetic properties of DMACuF are explained by the configuration of the magnetic orbitals. Magnetic lobes are found to run along the Cu-formate-Cu c-axis chains supporting strong SE interactions (J_{eq-eq}) between singly occupied magnetic orbitals, while along the $a + b$ and $a − b$ directions the singularly occupied orbitals on subsequent Cu^{II} ions are mutually orthogonal and therefore SE must involve a fully occupied orbital giving less efficient coupling (J_{eq-ax}). Accordingly, the Cu^{II} equatorial regions are rich in spin density.

An optimized crystal geometry was used to systematically compute the energy, E, of all possible colinear spin states (differences of FM and AFM spin alignments along J_{eq-eq} and J_{eq-ax}), where the energy of the system was described by

$$\hat{H} = \frac{1}{2}\sum_{R,R'} J(RR')\hat{S}_z(R) \cdot \hat{S}_z(R')$$

This journal is © The Royal Society of Chemistry 2020

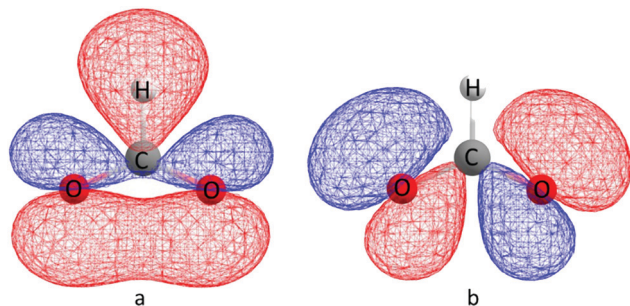*J. Mater. Chem. C*, 2020, **8**, 12840–12847 | **12845**

Fig. 7 (a) HOMO and (b) HOMO−1 molecular orbitals calculated for the isolated formate HCOO⁻ anion. The geometry was optimized, and the calculation run at the uB3LYP/6-311g(2d,2p) level of theory.
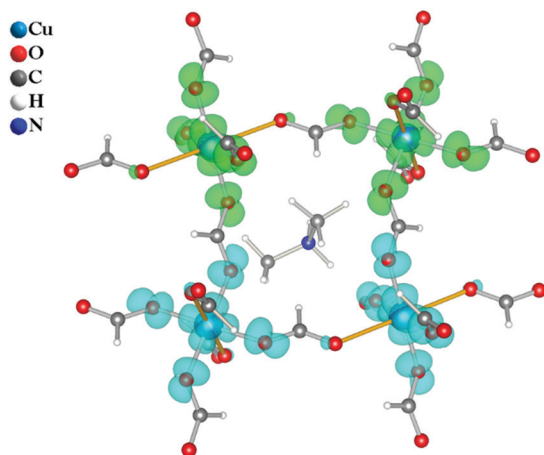

Fig. 8 Calculated spin density distribution represented at an isodensity value of 0.002 a.u. Green and cyan surfaces represent α (↑) and β (↓) spin densities. Yellow sticks represent JT elongated bonds.

with the spin operators S_z applied to ions at the R and R' lattice nodes. In qualitative agreement with the DFT calculations at the GGA+U level of theory by Wang *et al.*,[16] and with our experimental results presented above, the estimated J_{eq-eq} and J_{eq-ax} were found to be AFM and FM, respectively, with energies of +48.6 K and −2.0 K. We note that the magnitude of J_{eq-eq} was calculated to be approximately 2/3 of that determined experimentally. Such discrepancies are common for DFT calculations; however, the relative magnitude and sign are a robust result of this method. Given that $|J_{eq-eq}| > 10|J_{eq-ax}|$, these energies fully support the quasi-1D Heisenberg AFM nature of DMACuF.

Conclusions

Powder neutron diffraction and single crystal magnetometry experiments showed that DMACuF has an A_x-type magnetic structure below T_N, in which c-axis AFM chains are coupled ferromagnetically in the ab-plane, with magnetic moments aligned along the a-axis. Experimental charge density analysis found that the molecular electronic structure of the formate ligands that mediate both c-axis AFM and ab-plane FM superexchange was to a

good approximation the same, demonstrating the primary role of Cu–O bonding in establishing the nature of the exchange – in close analogy with inorganic perovskites. The charge density analysis was also used to reveal the electronic configuration of the Cu^{II} ions, which showed that for every Cu^{II} ion the singularly occupied d$_{x^2-y^2}$ orbital has lobes pointing along the c-axis, which facilitates a strong magnetic superexchange interaction, whereas along the in plane $a + b$ and $a − b$ directions the singularly occupied orbitals on subsequent Cu^{II} nodes are orthogonal to each other, greatly reducing the efficiency of the magnetic interaction. The spin density and magnetic exchange energies were estimated by density functional theory calculations, the results of which were fully consistent with the experimental magnetic structure solution and charge density analysis, and corroborated the quasi-1D magnetic properties of DMACuF evident in the field dependent magnetization. Importantly, the experimental determination of the magnetic and electronic structures together demonstrated that the GKA rules, widely used to predict the nature of magnetic exchange in the fully inorganic perovskites, are applicable to this class of hybrid organic–inorganic perovskite. For instance, based on the comparison of bond lengths and oxidation states the electronic properties of the symmetric eq–eq SE pathway in DMACuF are common to those found in Mn, Co, and Ni analogues. We suggest a maximal set of conditions for the ligand molecular orbitals that may guide the more general application of the GKA rules in all hybrid organic–inorganic materials.

Conflicts of interest

There are no conflicts to declare.

Acknowledgements

Notes and references

1 P. Wagner, G. Wackers, I. Cardinaletti, J. Manca and J. Vanacken, *Phys. Status Solidi A*, 2017, **214**, 1–25.
2 H. Liu and X. Yang, *Ferroelectrics*, 2017, **507**, 69–85.
3 D. I. Khomskii, *J. Magn. Magn. Mater.*, 2006, **306**, 1–8.
4 A. Maignan, C. Martin, S. Hébert and V. Hardy, *J. Mater. Chem.*, 2007, **17**, 5023–5031.
5 A. Hossain, A. K. M. Atique Ullah, P. Sarathi Guin and S. Roy, *J. Sol-Gel Sci. Technol.*, 2020, **93**, 479–494.
6 W. Li, Z. Wang, F. Deschler, S. Gao, R. H. Friend and A. K. Cheetham, *Nat. Rev. Mater.*, 2017, **2**, 1–18.
7 P. Jain, A. Stroppa, D. Nabok, A. Marino, A. Rubano, D. Paparo, M. Matsubara, H. Nakotte, M. Fiebig, S. Picozzi, E. S. Choi,

A. K. Cheetham, C. Draxl, N. S. Dalal and V. S. Zapf, *npj Quantum Mater.*, 2016, **1**, 16012.

8 A. Stroppa, P. Jain, P. Barone, M. Marsman, J. M. Perez-Mato, A. K. Cheetham, H. W. Kroto and S. Picozzi, *Angew. Chem., Int. Ed.*, 2011, **123**, 5969–5972.

9 H. L. B. Boström, M. S. Senn and A. L. Goodwin, *Nat. Commun.*, 2018, **9**, 2380.

10 C. S. Coates, H. J. Gray, J. M. Bulled, H. L. B. Boström, A. Simonov and A. L. Goodwin, *Philos. Trans. R. Soc., A*, 2019, **377**, 20180219.

11 G. Kieslich and A. L. Goodwin, *Mater. Horiz.*, 2017, **4**, 362–366.

12 M. Mączka, A. Gągor, M. Ptak, W. Paraguassu, T. A. da Silva, A. Sieradzki and A. Pikul, *Chem. Mater.*, 2017, **29**, 2264–2275.

13 S. Chen, R. Shang, K. L. Hu, Z. M. Wang and S. Gao, *Inorg. Chem. Front.*, 2014, **1**, 83–98.

14 K. L. Hu, M. Kurmoo, Z. Wang and S. Gao, *Chem. – Eur. J.*, 2009, **15**, 12050–12064.

15 Z. Wang, K. Hu, S. Gao and H. Kobayashi, *Adv. Mater.*, 2010, **22**, 1526–1533.

16 Z. Wang, P. Jain, K. Y. Choi, J. Van Tol, A. K. Cheetham, H. W. Kroto, H. J. Koo, H. Zhou, J. Hwang, E. S. Choi, M. H. Whangbo and N. S. Dalal, *Phys. Rev. B: Condens. Matter Mater. Phys.*, 2013, **87**, 224406.

17 P. J. Baker, T. Lancaster, I. Franke, W. Hayes, S. J. Blundell, F. L. Pratt, P. Jain, Z. M. Wang and M. Kurmoo, *Phys. Rev. B: Condens. Matter Mater. Phys.*, 2010, **82**, 012407.

18 J. B. Goodenough, *Phys. Rev.*, 1955, **100**, 564–573.

19 J. Kanamori, *J. Phys. Chem. Solids*, 1959, **10**, 87–98.

20 P. W. Anderson, *Phys. Rev.*, 1950, **79**, 350–356.

21 S. V. Streltsov and D. I. Khomskii, *Uspekhi Fiz. Nauk*, 2017, **187**, 1205–1235.

22 A. M. Glazer, *Acta Crystallogr., Sect. B: Struct. Crystallogr. Cryst. Chem.*, 1972, **28**, 3384–3392.

23 B. J. Campbell, H. T. Stokes, D. E. Tanner and D. M. Hatch, *J. Appl. Crystallogr.*, 2006, **39**, 607–614.

24 G. M. Sheldrick, *Acta Crystallogr., Sect. C: Struct. Chem.*, 2015, **71**, 3–8.

25 N. K. Hansen and P. Coppens, *Acta Crystallogr., Sect. A: Cryst. Phys., Diffr., Theor. Gen. Crystallogr.*, 1978, **34**, 909–921.

26 A. Valkov, P. Macchi, L. J. Farrugia, C. Gatti, P. Mallinson, T. Richter and T. Koritsanszky, XD2016, 2016.

27 P. J. Becker and P. Coppens, *Acta Crystallogr., Sect. A: Cryst. Phys., Diffr., Theor. Gen. Crystallogr.*, 1975, **31**, 417–425.

28 A. Ø. Madsen, *J. Appl. Crystallogr.*, 2006, **39**, 757–758.

29 R. Dovesi, R. Orlando, A. Erba, C. M. Zicovich-Wilson, B. Civalleri, S. Casassa, L. Maschio, M. Ferrabone, M. De La Pierre, P. D'Arco, Y. Noël, M. Causà, M. Rérat and B. Kirtman, *Int. J. Quantum Chem.*, 2014, **114**, 1287–1317.

30 E. Sletten and L. H. Jensen, *Acta Crystallogr., Sect. A: Cryst. Phys., Diffr., Theor. Gen. Crystallogr.*, 1973, **29**, 1752–1756.

31 E. F. Bertaut, *Magnetism*, Academic, New York, 1963, vol. III.

32 S. Chakravarty, B. I. Halperin and D. R. Nelson, *Phys. Rev. Lett.*, 1988, **60**, 1057–1060.

33 J. Brambleby, P. A. Goddard, R. D. Johnson, J. Liu, D. Kaminski, A. Ardavan, A. J. Steele, S. J. Blundell, T. Lancaster, P. Manuel, P. J. Baker, J. Singleton, S. G. Schwalbe, P. M. Spurgeon, H. E. Tran, P. K. Peterson, J. F. Corbey and J. L. Manson, *Phys. Rev. B: Condens. Matter Mater. Phys.*, 2015, **92**, 1–15.

34 R. F. W. Bader, *Atoms in molecules: a quantum theory*, Clarendon Press, 1990, p. 438.

35 R. Scatena, Y. T. Guntern and P. Macchi, *J. Am. Chem. Soc.*, 2019, **141**, 9382–9390.

36 P. Herich, L. Bučinský, M. Breza, M. Gall, M. Fronc, V. Petříček and J. Kožíšek, *Acta Crystallogr., Sect. B: Struct. Sci., Cryst. Eng. Mater.*, 2018, **74**, 681–692.

37 A. Holladay, P. Leung and P. Coppens, *Acta Crystallogr., Sect. A: Found. Crystallogr.*, 1983, **39**, 377–387.

38 M. J. Frisch, G. W. Trucks, H. B. Schlegel, G. E. Scuseria, M. A. Robb, J. R. Cheeseman, G. Scalmani, V. Barone, B. Mennucci, H. N. G. A. Petersson, M. Caricato, X. Li, H. P. Hratchian, A. F. Izmaylov, J. Bloino, G. Zheng, J. L. Sonnenberg, M. Hada, M. Ehara, K. Toyota, R. Fukuda, J. Hasegawa, M. Ishida, T. Nakajima, Y. Honda, O. Kitao, H. Nakai, T. Vreven, J. A. Montgomery. Jr., J. E. Peralta, F. Ogliaro, M. Bearpark, J. J. Heyd, E. Brothers, K. N. Kudin, V. N. Staroverov, R. Kobayashi, J. Normand, K. Raghavachari, A. Rendell, J. C. Burant, S. S. Iyengar, J. Tomasi, M. Cossi, N. Rega, J. M. Millam, M. Klene, J. E. Knox, J. B. Cross, V. Bakken, C. Adamo, J. Jaramillo, R. Gomperts, R. E. Stratmann, O. Yazyev, A. J. Austin, R. Cammi, C. Pomelli, J. W. Ochterski, R. L. Martin, K. Morokuma, V. G. Zakrzewski, G. A. Voth, P. Salvador, J. J. Dannenberg, S. Dapprich, A. D. Daniels, Ö. Farkas, J. B. Foresman, J. V. Ortiz, J. Cioslowski and D. J. Fox, *Gaussian 09*, 2009.

This journal is © The Royal Society of Chemistry 2020

J. Mater. Chem. C, 2020, **8**, 12840–12847 | 12847